Experimental CIGS technology performance under low concentration photovoltaic conditions

Miguel Barragán Sánchez-Lanuza [a,b], Isidoro Lillo-Bravo [b], Sara Moreno-Tejera [b], J.L. Sancho Rodríguez [c], Jose-Maria Delgado-Sanchez [a,*]

[a] *Dpt. Applied Physics I, University of Seville, Avda de Los Descubrimientos S/n, 41092, Seville, Spain*
[b] *Dpt. Energy Engineering, University of Seville, Ctra. Utrera Km 1, 41013, Seville, Spain*
[c] *Dpt. Technical Advisoring, Quintas Energy S.L., Avda. República Argentina 25, 41011, Seville, Spain*

A R T I C L E   I N F O

A B S T R A C T

This research study assesses the influence of the concentration factor on two different PV technologies: c-Si and CIGS, to analyze the feasibility of utilizing CIGS thin-film technology in Low Concentration Photovoltaic conditions. Additionally, the importance of the encapsulation design is explored to determine the optimum thermal management strategy. The initial phase involves an analysis of the thermal performance of two types of commercial photovoltaic module and explores the enhancement of temperature management in CIGS photovoltaics modules by substituting the rear glass backsheet with an aluminum sheet to reduce the operating temperature of the prototype. Subsequently, various prototypes are fabricated, incorporating CIGS and silicon technologies, and different encapsulation designs: tedlar, glass and aluminum backsheets. The analysis reveals that comparing performance under 2.2× and 1× concentration conditions, CIGS technology exhibits the higher performance at 2.2×, making it a more promising choice for LCPV systems. While CIGS technology boasts an intrinsic advantage because of its open circuit voltage temperature coefficient, its performance enhancement under LCPV conditions is further amplified through the optimization of the backsheet to improve the thermal management.

1. Introduction

Concentrated Photovoltaic (CPV) systems were conceptualized as an alternative to fixed stand photovoltaic (PV). These systems utilize optical elements to concentrate sunlight onto small, high-efficiency solar cells, resulting in higher energy yields compared to traditional flat-plate photovoltaic technologies (Shanks et al., 2016; Baharoon et al., 2015). Despite the potential advantages offered by High Concentration Photovoltaic (HCPV), several challenges hinder the development of new large-scale projects using this technology. Firstly, the high-quality optic components with high acceptance angle precision, typically Fresnel lens, impose a significant cost burden. Additionally, HCPV necessitate high-precision tracking mechanism to ensure optimal alignment with the sun, which adds complexity and further maintenance cost to these installations. Finally, although III-V solar cells demonstrate higher efficiency compared to conventional silicon cells, their production cost currently presents an obstacle in terms of the overall profitability of large-scale HCPV projects.

On the other hand, Low Concentration Photovoltaic (LCPV) systems (with concentration ratio below 10 suns) offer an economically viable alternative with consistently higher efficiencies compared to flat PV projects (Reis et al., 2010a; Parupudi et al., 2020). The reduced concentration level in LCPV minimize the cost of specialized optic components, allowing the use of simpler elements like flat mirrors or truncated parabolas. Furthermore, LCPV systems do not require high tracking precision contributing to overall cost reduction. Another advantage of LCPV design projects is their compatibility with a majority of solar cells technologies (Zahedi, 2011).

Effective thermal management is of paramount importance for the optimal performance and lifetime of photovoltaic (PV) systems and its components, especially in the context of low concentration photovoltaic (LCPV) systems. Thermodynamic principles (Shockley and Queisser) limit the efficiency of solar cells, leading to the conversion of some solar irradiance energy into heat. Currently, the electric conversion performance of a conventional silicon PV module in the market is around 13–22%. The excess solar radiation that is not converted into electricity contributes to an increase in the solar cell temperature, resulting in a decrease in electricity generation efficiency. If this heat is not properly managed, it can significantly impact the performance of the PV system

Nomenclature		J_0	Diode leakage current density
		k_B	Boltzmann constant
a	Ideality factor	LCPV	Low Concentration Photovoltaic
a-Si	Amorphous silicon	mc-Si	Polycrystalline silicon
CIGS	Copper–Indium–Gallium-Selenide	P_0	Nominal power of the system
CdTe	Cadmium telluride	PR	Performance ratio
CPV	Concentrated Photovoltaic	PV	Photovoltaic
c-Si	Monocrystalline silicon	q	Electrical charge
Cx	Concentration factor	STC	Standard Test Conditions
DNI	Direct normal irradiance	T	Temperature
E_{out}	Energy production	T_a	Ambient temperature
G_{POA}	Solar irradiation in plane	T_m	Photovoltaic module temperature
G_{STC}	Solar irradiation in Standard Test Conditions	V	Voltage
H	Finned heatsink height	V_T	Thermal voltage
HCPV	High Concentration Photovoltaic	V_{oc}	Open-circuit voltage
IEC	International Electrotechnical Commission Standard	WS	Wind speed
J	Current density	Y_f	Array field
J_{sc}	Short-circuit current density	δ	Power temperature coefficient

or even attempt its lifespan (Wang et al., 2020). The decline in performance due to rising PV module temperatures primarily stems from the reduction in the open-circuit voltage (V_{oc}), which exhibits a negative temperature coefficient. The PV module temperature affects the characteristics equation of the solar cell Eq. (1) in two ways (Luque and Hegedus, 2010): directly, through the exponential term involving temperature (T), and indirectly, via its impact on the dark photocurrent (J_0) which represents the diode leakage current density in the absence of light. While higher temperature reduces the magnitude of the exponent, the value of J_0 increases exponentially with T. Consequently, these combined effects lead to a linear reduction in V_{oc} Eq. (2) (Luque and Hegedus, 2010) as temperature increase (Shams, 2022).

$$J = J_{sc} - J_0 \left(e^{V/aV_T} - 1 \right) \qquad \text{[Eq. 1]}$$

$$V_{oc} = \frac{k_B T}{q} Ln \left(\frac{J_{sc}}{J_0} + 1 \right) \qquad \text{[Eq. 2]}$$

where J is the current density, J_{sc} is the short-circuit current, T the temperature, a the ideality factor, q the electrical charge, k_B the Boltzmann constant, V the voltage across the output terminals of the PV module, and V_T the thermal voltage.

Furthermore, PV module manufacturers typically offer product guarantees based on the International Electrotechnical Commission (IEC) Standard (Yolcan and Kose, 2023). This means that if the component operates at PV module temperature higher than 85 °C, the guarantee may become invalidated, thereby posing a significant risk to the owner of the PV plant (Nyarko et al., 2019).

Moreover, effective management of the incident flux on the solar cells is crucial to ensure uniform distribution. Non-uniform illumination can lead the formation of hotspots (Wang and Xuan, 2020), which in turn can cause irreversible damage to the solar cells, resulting in reduced power output of the panel over its lifetime.

Numerous reports in the literature discuss the design and analysis of LCPV systems (Yadav et al., 2013; Kolamroudi et al., 2022; Mansoor et al., 2020). For instance, Famoso et al. (2015) developed an LCPV prototype utilizing c-Si solar cells, with a concentrating system comprising plastic truncated cones covered by a metal film reflecting the radiation directly on the basis of the lenses where the solar cells were installed. Their study concluded that the performance ratio of the LPCV system surpassed that of fixed-angle PV systems, particularly in regions at latitudes with higher values of direct normal irradiance (DNI) solar radiation. Saini et al. (2018) analyzed a design featuring of a compound parabolic concentrator integrated with a photovoltaic thermal collector,

incorporating various solar cell technologies, such as monocrystalline (c-Si), polycrystalline (mc-Si) and amorphous silicon (a-Si), cadmium telluride (CdTe), and copper-indium-gallium selenide (CIGS). They pointed out that the compound parabolic concentrator produced a non-uniform light on the solar cells, leading to hot spots on the PV module, especially at high incident angles. Additionally, Reis et al. (2010b) modeled the performance of LCPV systems using silicon solar cells and V-trough reflectors consisting of two mirrors to achieve 2× concentration factor.

The majority of the previous cited references focus on the silicon solar cells. However, thin-film technologies are achieving efficiencies comparable to silicon solar cells and offer additional advantages, such as flexible and low weight substrates that positively impact tracker design. Another design advantage is that they are manufactured using the monolithic integration process (Wennerberg et al., 2000). This means that in case of non-uniform illumination, the output power reduction is lower compared to silicon PV modules. In conventional silicon modules, the solar cells are connected in series, indicated by the yellow dotted line (Fig. 1), so the output power is dictated by the cell with the lowest current. Therefore, if certain solar cells experience lower illumination like Fig. 1a, the module performance is limited by the generation of these cells. On the other hand, as depicted in Fig. 1b, all cells span across the full-length module, ensuring that the current generation is equally affected for all solar cells (Oufettoul et al., 2023).

Wennerberg et al. (2000) developed an LCPV prototype using a compound parabolic concentrator and CIGS solar cells. Indoor measurements at up to 4× concentration factor demonstrated that CIGS technology is less sensitive to non-uniform defects compared to silicon solar cells. Similarly, Ward et al. (2002) explored the potential of using CIGS solar cells under LCPV conditions, achieving a performance of 21.5% at 4× concentration factor in a device of 0.1 cm². They emphasized the advantage of CIGS technology in competing against silicon solar cells due to the versatility of substrates used, such as flexible stainless steel with better management of thermal phenomena. However, this result was obtained through indoor facilities, and further validation is still pending through pilot projects in real operating conditions. Since that experiment, no major experiments have been reported using CIGS technology as selected device in the LCPV system. More recently, Cherif and Sammouda (2022) simulated one tandem perovskite-CIGS solar cell operating under LCPV conditions, but this work has not yet been validated experimentally.

Continuous research and further experimental validation in this direction hold the potential to stablish CIGS-based LCPV systems as competitive and complementary alternative to traditional silicon-based
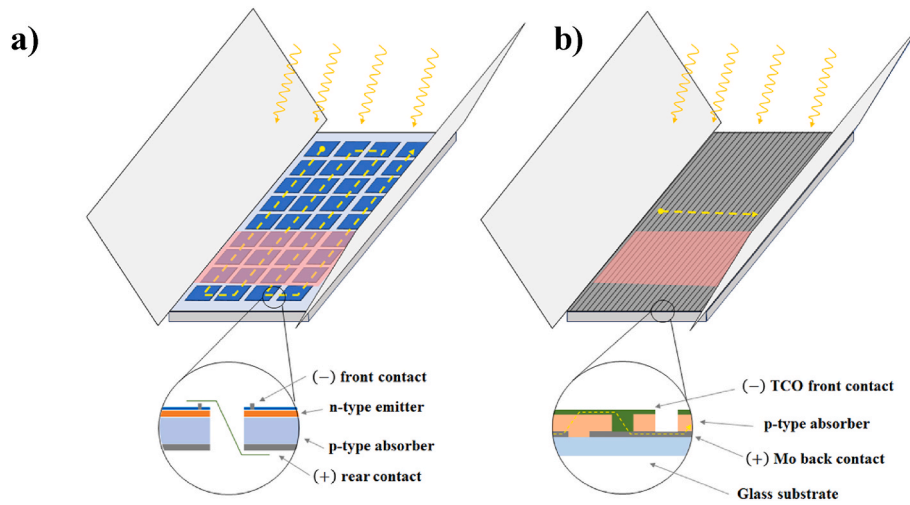
Fig. 1. Schematic drawing of a conventional silicon PV module (a) and CIGS thin film module (b) under non-uniform illumination conditions. (For interpretation of the references to colour in this figure legend, the reader is referred to the Web version of this article.)

technologies in the solar energy landscape. This research aims to design and evaluate three LCPV prototypes under real outdoor operating conditions to investigate the performance dependence on the PV technology and the type of encapsulation. The first prototype utilizes silicon solar cells, while the remaining two employ CIGS technology, one with monolithic integration and the other with independent solar cells connected in series, similar to the silicon prototype. Each type of prototype considers different backsheets in the encapsulation to evaluate its influence on the output power generated.

By comparing the performance of these prototypes, the study looks to identify the most efficiency design for managing thermal losses and assessing the impact of non-illumination impact on the electricity generation for each case. To ensure compliance with the manufacturer guarantee, a control system has been implemented in the tracker to avoid that the temperature of the PV module remains below 85 °C. The data collected from these LCPV prototypes will provide valuable insights into optimizing their performance, advancing our understanding of CIGS-based solar cells, and contributing to the broader goal of enhancing solar energy technologies.

2. Methods description

2.1. Performance characterization

The research entails a comparative analysis of two different solar cell technologies, their specific encapsulation design, and aims to assess their disparities by taking into account various factors, such as PV module size, tilt and azimuth angle, received irradiation, and prevailing weather conditions over multiple days. By employing quality normalized indicators, a comprehensive and unbiased evaluation of the solar cell technologies can be conducted, facilitating a deeper understanding of their performance characteristics under different environmental conditions.

The Array Yield (Y_f) is characterized as the ratio between the energy production (E_{out}) and the nominal power of the system (P_0) (Woyter et al., 2014). This particular indicator holds the benefit of standardizing the energy production relative to the system capacity size, thus enabling direct comparisons among prototypes with varying peak capabilities.

$$Y_f = \frac{E_{out}}{P_0} \qquad \text{[Eq. 3]}$$

The Performance ratio (*PR*) allows the quantification of system losses arising from different factors such as spectral mismatch, PV module temperature variation, and other system malfunction. While various

methodologies exist to evaluate the *PR*, this analysis compares the conventional procedure (Khalid et al., 2016) described in Eq. (4) with the weather-corrected approach originally proposed by NREL (Dierauf et al., 2013), described in Eq. (5), which has also been endorsed by the IEC in the last years and take in consideration the PV module temperature effect.

$$PR = \frac{\frac{E_{out}}{P_0}}{\frac{G_{POA}}{G_{STC}}} \qquad \text{[Eq. 4]}$$

$$PR^* = \frac{E_{out}}{P_0 \cdot \frac{G_{POA}}{G_{STC}} \cdot \left[1 - \frac{\delta}{100} \left(T_{cell,avg} - T_{cell,i} \right) \right]} \qquad \text{[Eq. 5]}$$

$$T_{cell} = T_m + \frac{G_{POA}}{G_{STC}} \cdot \Delta T_{cnd} \qquad \text{[Eq. 6]}$$

$$T_m = G_{POA} \cdot e^{(a+b \cdot WS)} + T_a \qquad \text{[Eq. 7]}$$

where G_{POA} represents the solar irradiation in plane, G_{STC} is the solar irradiation in Standard Test Conditions (STC), E_{out} is the energy out, δ is the power temperature coefficient of the solar cell, *WS* is the wind speed, T_a and T_m represents the ambient and PV module temperature, *a* and *b* are empirical constants related to the temperature increase due to reflected sunlight, and finally ΔT_{cnd} is a coefficient defined by the type of encapsulation of the PV module (Dierauf et al., 2013).

2.2. Prototype design

Under LCPV conditions, three design types are juxtaposed: the conventional c-Si PV module, a glass-glass conventional CIGS thin-film PV module, and a novel alternative CIGS thin-film PV module incorporating glass and aluminum encapsulation aimed at mitigating thermal losses. This section undertaken a comprehensive analysis of the distinct components integral to the LCPV prototypes.

Balancing cost and optical performance, it has been selected flat mirrors as reflectors to concentrate solar energy onto the LCPV prototypes for this research case, using a V-trough configuration inclined by an angle (*θ*) as illustrate in Fig. 2. The key considerations for selecting the optimal optic system are: (1) material reflection should closely match the spectral response of the solar cell to maximize energy capture; (2) reflectivity must be as higher as possible to enhance light concentration; (3) the reflector material and its support structure should be cost-effective to ensure feasibility of the LCPV system; (4) the manufacturer must guarantee reflectivity throughout the entire lifetime of the
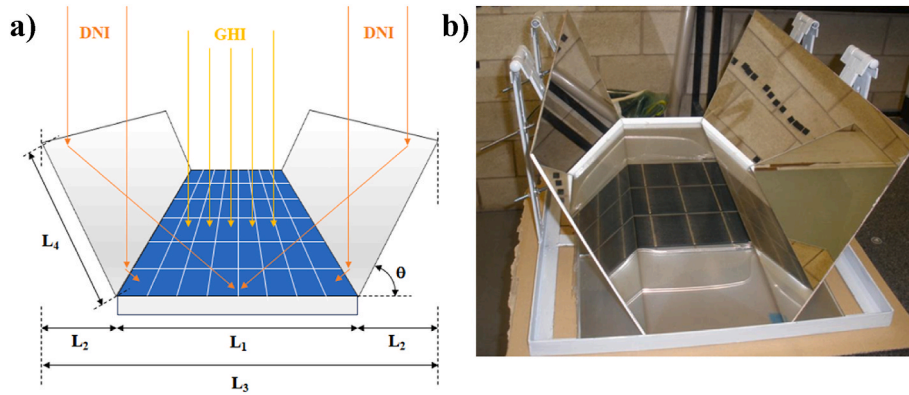
Fig. 2. a) Schematic drawing for design mirror geometrical parameters; b) Photography of one prototype during its manufacturing.

LCPV system to maintain optimal performance; (5) the reflector's mechanical construction should be straightforward and robust enough to withstand various climatic atmospheric events (strong wind loads, vibrations, thermal expansion, etc.)

The objective of the LCPV design in this study is to achieve a concentration factor (C_x) of 2.2×. By considering the PV module parameters (Table 1) and utilizing Eq. (8) and Eq. (9), the angle (θ) and height (L_4) of the mirror required for each prototype were determined (Oufettoul et al., 2023).

$$C_x = \frac{S_3}{S_1} = \frac{L_3}{L_1} = 2.2x \Rightarrow L_3 = 2.2 \cdot L_1 \qquad \text{[Eq. 8]}$$

$$\theta = cos^{-1}\left(\frac{L_2}{L_4}\right) = cos^{-1}\left(\frac{L_3 - L_1}{2L_4}\right) \qquad \text{[Eq. 9]}$$

In the selection of an appropriate mirror material for the LCPV prototype, metals that exhibit free electron-like behavior and adhere to the Drude model are considerable suitable (Lee et al., 2023). Among these options, silver and aluminum are prominent candidates, with typical solar hemispherical integrated reflectivity values of 94% and 91%, respectively, covering the spectral range from 300 to 2500 nm. However, it is important to note that the spectral response of silicon and CIGS solar cells are limited to the range from 400 to 1100 nm (Fernández-Solas et al., 2021). Consequently, energy reflected beyond 1100 nm does not contribute to the photoelectric conversion process but rather results in thermal losses that must be managed properly to avoid performance losses in the PV system. Unfortunately, no metals are available that combine low reflectance in the NIR-IR range with high reflectance in the UV-VIS range, which aligns with the specific spectral response of the solar cells. Additionally, a crucial consideration is the potential degradation of the reflector material. In comparison, the degradation of silver occurs at a faster rate than that of aluminum (Grosjean et al., 2021). Balancing these optical properties, chemical stability, and cost factors, aluminum glass mirrors have been selected for this research case, boasting a total reflectivity of 93%.

The PV technology chosen for these prototypes is thin-film CIGS. The

first set of prototypes utilizes conventional c-Si PV modules manufactured by Jinko, featuring an encapsulation structure comprising a glass-tedlar combination. The second set employs CIGS PV modules provided by Würth Solar, characterized by a glass-glass encapsulation. Lastly, the final set of prototypes incorporates CIGS solar cells supplied by Global Solar, which undergo lamination with a glass-aluminum. Further technical details regarding the commercial PV modules are disclosed in Table 2.

2.3. Thermal model CIGS glass – aluminum

To further enhance thermal management within our prototypes operating under LCPV conditions, we have undertaken a comprehensive modeling approach using NX 6.0 S PLM software. This modeling enables us to anticipate and evaluate the thermal performance discrepancies expected between different prototype design, and to identify and incorporate the most effective thermal dissipator elements on the rear surface of the device. For this modeling phase, a finite element analysis (Fig. 3) approach was employed utilizing thin shell elements (2D) for flat surfaces, such as the front glass and the intermediate layers of the CIGS thin-film solar cell, and solid elements (3D tetrahedra) for the heat dissipator component. The element size chosen for the thin shell elements was approximately 0.5 mm, while for the solid elements, it was approximately 2 mm. This meticulous selection of element sizes resulted in the generation of a fine mesh, allowing for the precise identification and analysis of potential temperature gradients within the prototype. A grid independency test was carried out by progressively increasing the number of elements until the maximum temperature difference between two consecutive sets of grids was less than 0.1%. This analysis ensure that the developed model is independent of grid size when predicting the solar cell temperature. Referring to Fig. 3, while maintaining a balance between computational efficiency and prediction accuracy, it is observed that for a number of elements greater than 240,000 the temperature difference is less than 0.1 %. At this stage, the solution was deemed grid independent and converged.

Due to the thinness of the layer comprising the CIGS solar cells, with a thickness measuring less than 2 μm, it is assumed that there exists perfect thermal contact between the glass and the solar cell, as well as

Table 1

Geometric specifications for each V-through reflector ensuring a concentration factor of 2.2x.

Prototype	PV module		Mirror	
	Width L_1 (mm)	Length L_0 (mm)	Height L_4 (mm)	Length L_0 (mm)
c-Si solar cells in series	800	1650	1760	1650
CIGS monolithic integration	600	1200	1320	1200
CIGS solar cells in series	210	500	462	500

Table 2

Commercial PV Module datasheet.

	c-Si	CIGS glass-glass	CIGS glass-aluminum
Voc (V)	38.0	45.5	3.1
Isc (A)	8.92	2.50	5.9
Vmp (V)	30.8	36.0	2.3
Imp (A)	8.28	2.22	5.7
Peak power (W)	255	80	13
Temp. Coeff. of V (V/°C)	−0.118	−0.299	−0.299

Fig. 3. Variation of temperature as function of the number of grid elements.

Table 3
Thermal and optical properties of the materials forming LCPV prototype.

Material	Thermal conductivity (W·m^{-2}·K)	Emissivity	Absorbance (%)	Transmittance (%)
Glass	1	0.84	1.8	89.9
CIGS solar cell	27	0.31	83.6	0
Aluminum	209	0.84	14.2	0

Fig. 5 presents the initial outcomes derived from the thermal modeling. These results demonstrate a direct correlation between the concentration factor and the increase in solar cell temperature. Notably, the aluminum backsheet exhibits superior heat dissipation capabilities compared to the rear glass, resulting in lower solar cell temperatures when integrated into the prototype design. To point out the high temperature gradient observed in the glass-glass prototype that even might induce the glass cracking. Furthermore, it is noteworthy that under LCPV conditions the estimated solar cell temperatures align more closely with the maximum recommended operating temperature of 85 °C as stipulated in the IEC Standards. However, it is essential to emphasize that this threshold is exceed when the prototype incorporates glass as backsheet material. These findings underscore the necessity of introducing additional design considerations and parameters in the prototype development phase to ensure their reliability and compliance with the manufacturer's warranty conditions, thereby mitigating the risk of potential operational failures.

A significant additional design consideration for the prototypes employing aluminum backsheets is the assessment of the impact of incorporating finned heatsinks on the solar cell temperature. To address this, a second thermal modeling analysis was conducted, focusing on determining the optimal height of the finned heatsinks. The summarized results of this simulation are presented in Table 4. The findings of this second thermal modeling revealed a notable trend. The inclusion of finned heatsinks within the design leads to a substantial reduction in solar cell temperatures. Specially, in the case of the glass-glass design, the solar cell temperature stands at 125 °C, whereas incorporating a glass-aluminum sheet in the rear side lowers it to 89 °C. However, the most significant reduction is achieved when both the glass-aluminum backsheet and finned heatsinks are employed together, resulting in a remarkable decrease to 47 °C. Furthermore, it is essential to note that this integration of finned heatsinks not only substantially lowers the overall temperature but also plays a crucial role in minimizing the temperature gradient across the solar cell, as evidenced in Fig. 6. These results underscore the critical importance of considering finned heatsinks as an integral component in the design phase. Based on these findings, CIGS prototypes manufactured in this research study considered the following backsheets: Type I, which consists of 4 mm-thick glass, and Type II comprising 3 mm-thick aluminum with a finned heatsink that has a height of 10 mm and is spaced 50 mm apart. The finned heatsink used is cost effective solution and does not require the use of forced refrigeration system.

between the glass and the aluminum backsheet. In modeling the convection process, natural convection to ambient conditions has been considered, with a convection coefficient of 3.4 W m^{-2}·K, representing the worst-case scenario in which wind speed is null. This hypothesis also extends to the external glass surface, as well as both the external and internal surfaces of the heat dissipator (Fig. 4). Notably, the internal temperature within the heat dissipator (T_0) remains undefined and is contingent upon the temperature distribution across the prototype. Concerning radiation mechanisms, three distinct boundary conditions have been taken into account: heat exchange between the glass and the front face of the heat dissipator with the sky, following the utilization of the Swinbank Eq. (10) (Yang et al., 2020):

$$T_{sky} = f_n \cdot T_{amb} + 0.0552 \cdot (1 - f_n) \cdot T_{amb}^{1.5} \qquad \text{[Eq. 10]}$$

where f_n represents the cloudiness factor, taking values within the range of 1 (completely overcast day) to 0 (perfect clear sky). Our findings indicate that under clear sky conditions ($f_n = 0$) and during the peak of summer when ambient temperature can reach 42 °C, the sky temperature (T_{sky}) was observed to be 15.3 °C. It is worth noting that the other surfaces of the heat dissipator interact with the ambient environment through radiation mechanisms. Furthermore, we have made the assumption that radiation exchange within the heat dissipator itself can be neglected, based on the hypothesis that the temperature within the element remains sufficiently uniform. Properties of the materials considered for the modeling are described in Table 3.
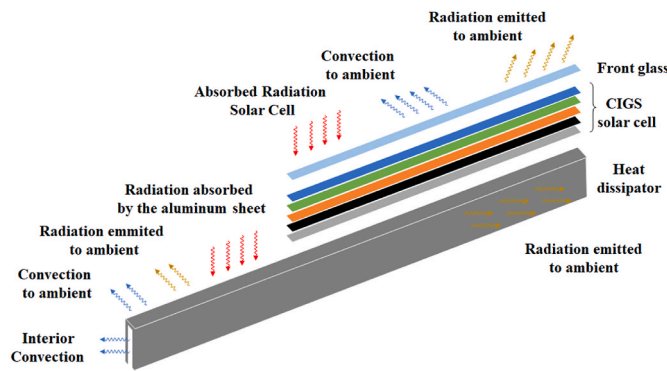
2.4. Characterization equipments

Reflection and transmission coefficients required for the thermal model have been obtained using a UV-VIS spectrophotometer (Agilent, Cary 4000), while emissivity has been obtained in a TIR 100–2 (Inglass) emissometer as the reflectivity of radiation emitted at 100 °C, and derived from the sheet resistivity measured with an inductive sheet resistivity meter (Nagy SRM-12).

The electrical outdoor characterization of the LCPV prototypes is conducted employing an IV tracer (PVE model PVPM 1000 C[40] calibrate with a reference solar cell which ensures an accuracy of ± 2 W).

The temperature of the prototypes is monitored through some PT100

Fig. 4. Prototype structure employed in the finite element thermal modeling to design the heat dissipator.
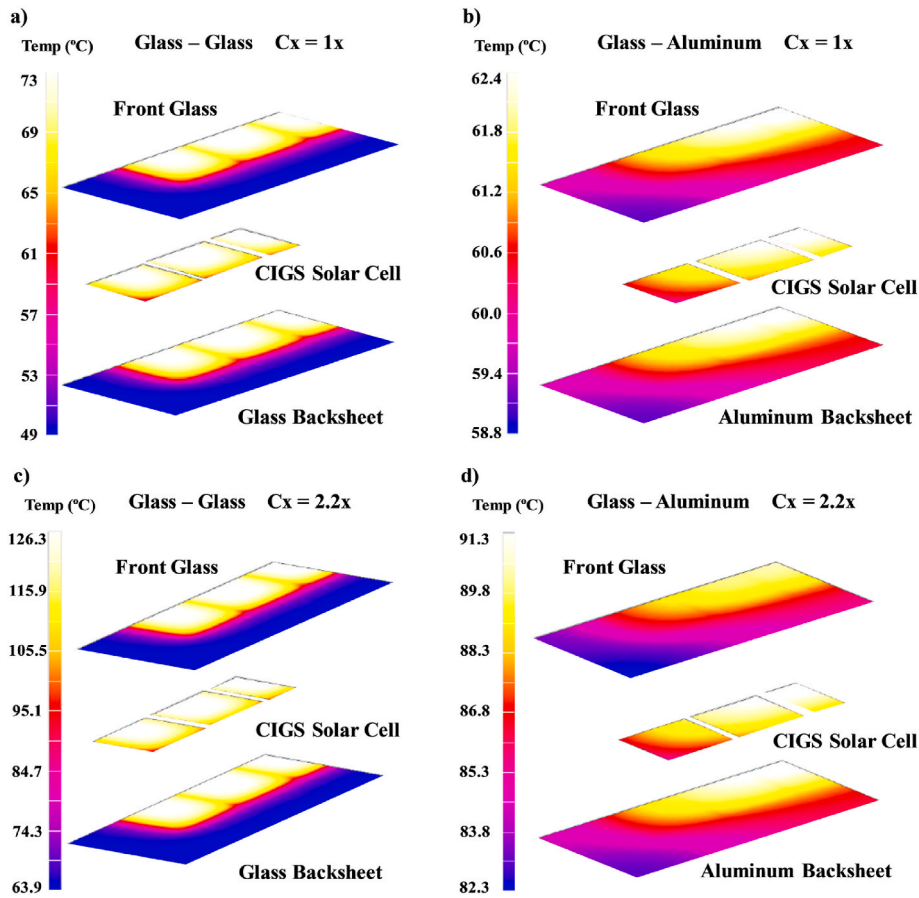
Fig. 5. Temperature distribution modeled considering two types of backsheet in the prototype: glass (a,c) and aluminum (b,d), both under 1× and 2.2× concentration factor.

Table 4
Finned heatsink height influence on the overall solar cell temperature under different concentration factor.

Cx	H = 0	H = 10 mm	H = 15 mm	H = 20 mm	H = 25 mm
1×	60	45	44	44	44
2.2×	89	47	47	46	45
5×	135	51	49	48	47
20×	279	70	65	61	58

accuracy ± 0.3 °C. Temperature distribution is evaluated using a thermography camera (Flir model C2 with thermal sensitivity of 0.1 °C and an accuracy of ± 2 °C).

Environmental conditions, including solar irradiance (+/2%), ambient temperature (± 0.3 °C), wind speed (± 0.3 m/s), and direction (± 3°), are measured at 5-min intervals utilizing a meteorological station (Geonica MTD 301). This station, equipped with sun tracking capability, incorporates 2 Kipp & Zonen piranometers and 1 pyrheliometer to provide comprehensive meteorological data.
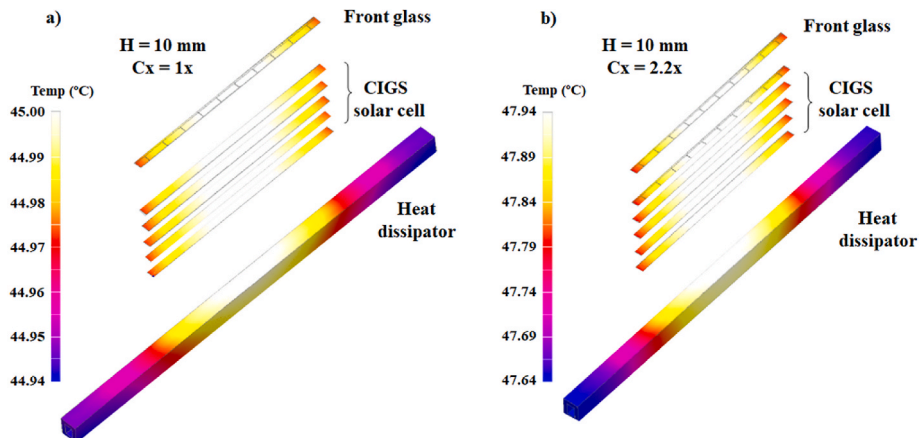
Experimental facilities are located in Seville (Spain).

probes connected to a datalogger (Agilent 34970 A) ensuring an

Fig. 6. Temperature gradient simulated with (a) and without (b) concentration factor applied (2.2×) when the prototype is designed with finned heatsinks.

3. Results and discussion

3.1. Temperature influence characterization

The primary objective of this experimental phase was to assess the prototype's power output as function of varying ambient temperature and solar irradiance level. To ensure precise alignment of the mirrors, thereby attaining the specific 2.2× concentration factor, all LCPV prototypes were securely affixed to a 2-axis tracking system. The experimental setup involved the continuous monitoring of environmental parameters including the temperature of the PV modules (Fig. 7). During the monitoring campaign, the average ambient temperature was 27 °C and wind speed was lower than 1.5 m/s. As previously mentioned, ensuring the reliability of PV modules in accordance with the manufacturer's warranty is crucial. One essential aspect is the monitoring of module temperatures to prevent them from exceeding 85 °C. To address this concern, the 2-axis tracker incorporates a higher level of control. When the temperature of the PV module exceeds 85 °C, the tracker adjusts its position to reduce the concentration factor, thereby preventing overheating and ensuring compliance with the manufacturer's warranty terms as specified in the IEC standard.

In Fig. 8, it is showed the relative temperature difference of PV modules operating with and without LCPV conditions as function of the irradiance (G) on the prototype, the DNI available, and the concentration factor (C_x): $G = DNI \times C_x$. For instance, when DNI is 500 W m^{-2}, it means that the prototype operating at 1× receives $G = 500 \times 1x = 500\ W \cdot m^{-2}$, and the prototype at 2.2× receives $G = 500 \times 2.2x = 1100\ W \cdot m^{-2}$. It is observed notable distinctions in the thermal behavior when prototypes operate at a concentration factor of 2.2×. At 2.2× CIGS glass-glass maximum temperature was 81 °C, while CIGS glass-aluminum remained at 62 °C. c-Si remains within this range closer to glass-aluminum. Experimental data for c-Si and CIGS glass-glass prototypes exhibits a high level of concordance with the Sandia PV module temperature model (Peng et al., 2015). This model accounts for various factors, including ambient temperature, wind speed, solar irradiance, and the type of backsheet employed in the prototype. Given the uniformity of ambient conditions across all monitored prototypes, the principal determinants of PV module temperature variation are attributed to the semiconductor technology employed and the specific design

characteristics of the backsheet. However, CIGS glass-aluminum cannot be compared to Sandia model because it has not yet undergone experimental validation for glass-aluminum encapsulation with CIGS solar cells.

When comparing the prototypes tested, it becomes apparent that c-Si technology exhibits the highest PV module temperature difference between 1× and 2.2× conditions, with a notable 32% average increase at maximum irradiance level. This substantial rise can be attributed to its high Voc temperature coefficient. Following closely behind, the CIGS glass-glass encapsulation shows a maximum average increase of 27% temperature difference, while the CIGS glass-aluminum encapsulation displays a maximum average increase of 17% difference. It is evident that while CIGS technology benefits from its Voc temperature coefficient when operating under higher irradiance levels than STC conditions, the choice of encapsulation materials plays a crucial role in minimizing thermal losses. The experimental data shown in Fig. 8, along with the ambient temperature presented in Fig. 7, align well with the predicted temperature displayed in Fig. 5. Consequently, this experiment also serves as validation of the thermal model.

In the pursuit of optimizing the performance of any PV technology operating under LCPV conditions, understanding the thermal characteristics of the PV modules is of paramount importance (Li et al., 2018). To comprehensively assess the thermal distribution of these prototypes, a grid of thermocouples was meticulously positioned on the rear side of each prototype. These temperature measurements were recorded at regular intervals of 200 mm across the prototype rear surface. We observed that all PV technologies exhibited a nearly homogeneous thermal distribution. At the center of each prototype, we observed the highest temperature values, which gradually slightly decreased as we moved closer to the edges, as it was expected. Remarkably, the highest temperature difference between those points remained consistently below 3% for all the prototypes tested. This uniformity in PV module temperature distribution is a promising indicator of the robustness and reliability of the prototypes manufactured. Fig. 9 illustrates the temperature distribution results obtained for a specific prototype employing CIGS technology with glass-glass encapsulation configuration. However, during our measurement campaign, a noteworthy anomaly was found. As depicted in Fig. 9b, one of the samples exhibited a significant non-uniform temperature pattern when compared to a similar one
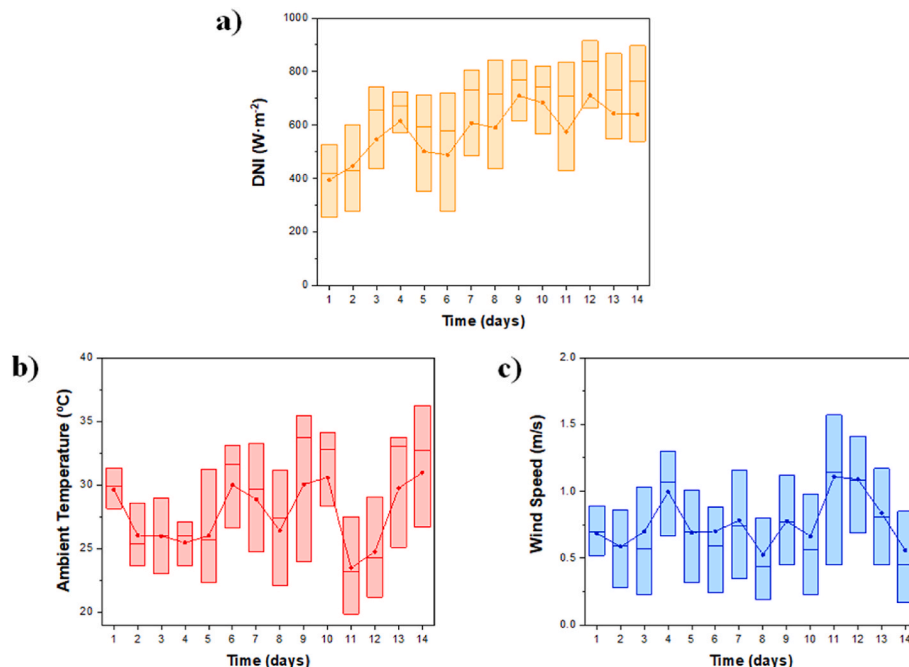

Fig. 7. Ambient conditions monitored for the sun hours during the test campaign: a) DNI measured on the tracker; b) Ambient temperature; and c) wind speed.
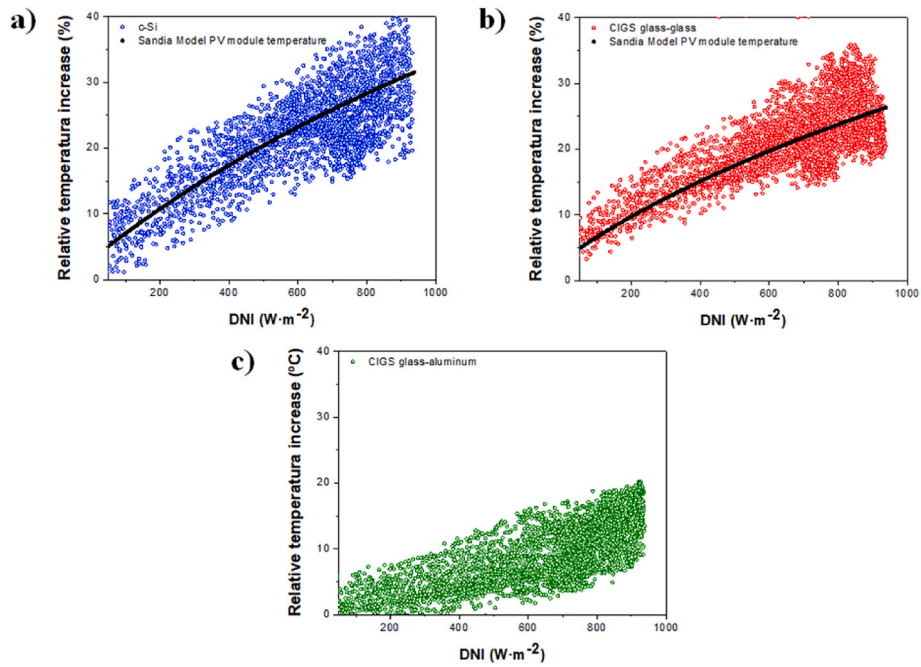
Fig. 8. PV module temperature relative difference for each prototype operating at Cx = 1× and Cx = 2.2×: a) c-Si (blue); b) CIGS glass-glass (red); c) CIGS glass-aluminum (green). (For interpretation of the references to colour in this figure legend, the reader is referred to the Web version of this article.)
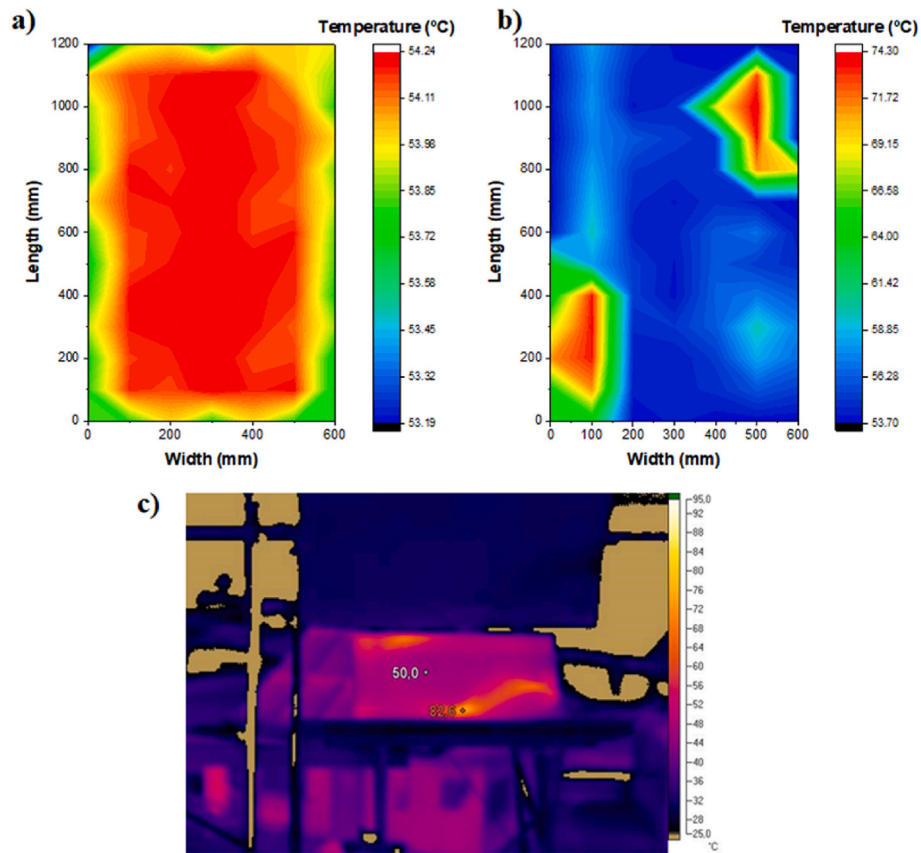

Fig. 9. Temperature distribution on CIGS glass-glass prototype (a); similar prototype with non-uniform temperature distribution (b) due to a failure in the mirrors; thermography image to understand the root-cause of this failure (c).

(Fig. 9a). To gain deeper insights into this irregularity, Fig. 9c shows a thermography image to investigate the root-cause of this failure. This thermal anomaly was linked to imperfections in the flatness of the mirrors used in this prototype. This particular sample, which demonstrated uneven PV module temperature distribution, was subsequently excluded from the research study, because according to Fig. 1, the

non-homogeneous radiation on the prototype affects the overall performance.

3.2. Output power characterization

The outdoor current-voltage (I–V) curve characterization results is summarized in Table 5 and Fig. 10. STC data are compared to outdoor measurements extrapolated in accordance with the IEC 60891:2021. It becomes apparent that the short-circuit current (Isc) demonstrates a direct correlation with the incident radiation for all tested PV technologies, surpassing not only the STC values but also the values obtained without any concentration factor, both for c-Si and CIGS. However, a notable divergence becomes evident when scrutinizing the Voc. The Voc of the c-Si technology exhibits a more pronounced reduction compared to the prototype of CIGS, a phenomenon attributable to its higher temperature coefficient. The CIGS glass-aluminum prototype exhibits a lower Voc reduction compared to the CIGS glass-glass prototype, due to its better thermal management design in the backsheet. It's worth noting that LCPV operational conditions invariably result in elevated PV module temperatures, a factor that notably impacts the output power of c-Si technology (86 % enhancement) in comparison to CIGS (103% and 113%). Consequently, the results gleaned from the I–V curves support the assertion that CIGS technology is intrinsically recommended for LCPV applications, because the elevated PV module temperatures achieved have a lower voltage reduction.

To assess the electrical performance of the LCPV system, we monitored the DC output power generated as function of the irradiance. Fig. 11 presents a comparative analysis of the results obtained for the distinct prototypes developed within this research study. By employing the model proposed by Huld et al. (2010) (Eqs. (11) and (12)), we observe a robust alignment between the model predictions and the experimental data collected for all the tested technologies.

$$P(G, T_{mod}) = P_{STC} \cdot \frac{G}{G_{STC}} \cdot \eta_{rel}(G', T') \qquad \text{[Eq. 11]}$$

$$\eta_{rel}(G', T') = 1 + k_1 \, Ln \, G' + k_2 (Ln \, G')^2 + T'(k_3 + k_4 \, Ln \, G' + k_5 (Ln \, G')^2)$$
$$+ k_6 T'^2 \qquad \text{[Eq. 12]}$$

where P_{STC} is the power at STC with $G_{STC} = 1000 \, W \cdot m^{-2}$ and $T_{STC} = 25 \,°C$. $\eta_{rel}(G', T')$ is the instantaneous relative efficiency, and G' and T' are normalized parameters to STC values: $G' = G/G_{STC}$ and $T' = T_{mod} - T_{STC}$. The coefficients $k_1 - k_6$ are experimentally determined and can be found in references (Huld et al., 2010, 2011) for c-Si and CIGS PV technologies.

The Huld model depicted by the black dots in Fig. 11 estimates the anticipated losses resulting from each parameter compared to the reference STC conditions (represented by the green dots in Fig. 11). Given the semiconductor nature of the material, the cell exhibits a negative temperature coefficient of Voc, and this reduction in Voc serves as the explanation for the observed decrease in output power when compared to the expected values under STC reference conditions. Pointing out that not all prototypes employ the same PV technology, and

their encapsulation designs differ as well, thermal losses affect them to varying degrees. For instance, when comparing experimental data under LCPV conditions to the STC reference conditions, the c-Si prototype exhibits the highest average power losses (34%) at maximum irradiance level. It is followed by the CIGS glass-glass (29%) and CIGS glass-aluminum (20%) prototypes.

The high Voc temperature coefficient of c-Si technology elucidates its limitations in operating under high temperature. The disparity with the CIGS glass-glass prototype, while significant, is not enormous. This can be attributed to the fact that, despite CIGS having a lower Voc temperature coefficient than c-Si, the glass-glass encapsulation offers inferior thermal performance compared to the glass-polymer backsheet used in the c-Si prototype. The CIGS glass-aluminum prototype showcases an optimal design for operation under LCPV conditions. Its low Voc temperature coefficient, combined with an effective heat dissipation design on the rear side, underscores its capability to operate optimally in the LCPV context.

3.3. Performance analysis

The most suitable performance metrics for characterizing the comprehensive performance of LCPV systems concerning energy generation and prevailing environmental conditions are array yield and performance ratio. The synthesis of the standardized performance, derived from an outdoor experimental evaluation spanning a period of 14 days, is graphically illustrated in Fig. 12.

Y_f and PR reveal similar values for all prototypes at $1\times$ (63, 64, and 67 W h/W_p) for c-Si, CIGS glass-glass, and CIGS glass-aluminum, respectively. However, at a concentration factor of $2.2\times$, Y_f increases significantly in the CIGS glass-aluminum prototype (74%), while c-Si and CIGS glass-glass show enhancements of 59% and 62%, respectively. This reduction is attributed to limitations in the heat management. PR at $2.2\times$ is lower than PR at $1\times$, with the most significant losses observed in c-Si (11%). Once again, the encapsulation chosen for CIGS glass-aluminum ensures that PR only decreases 3%.

4. Conclusions

This research study focused on the influence of the concentration factor on two different PV technologies (c-Si and CIGS), and the encapsulation materials. Our findings consistently demonstrated that CIGS technology outperforms c-Si in LCPV conditions: The CIGS glass-aluminum encapsulated prototype achieved a PR of 74%, surpassing the c-Si counterpart which attained 70%, both under a concentration factor of $2.2\times$. Furthermore, the specific array of the CIGS glass-aluminum encapsulated demonstrated a 17% improvement compared to the c-Si prototype (59%) under identical operating conditions. The primary contributing factor to this superiority is the lower Voc temperature coefficient exhibited by CIGS thin-film PV modules. This intrinsic characteristic enables CIGS to maintain its efficiency advantage under higher irradiance levels, making it an appealing choice for LCPV applications.

Moreover, this research underscored the critical role of encapsulation in minimizing thermal losses. Specifically, when replacing the rear

Table 5
STC and outdoor I–V curve characterization of the LCPV prototypes.

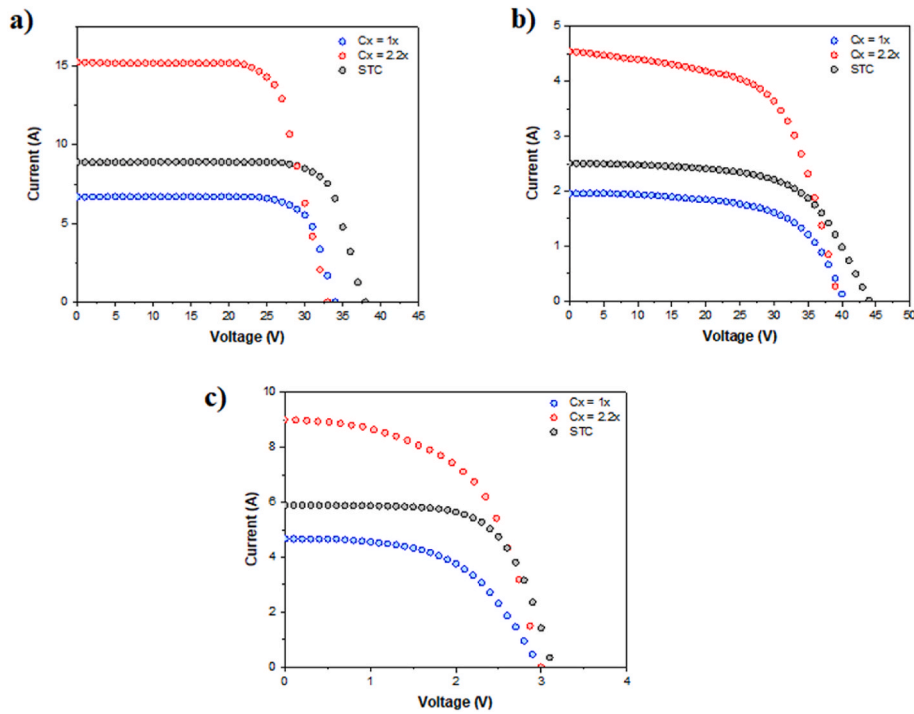|	c-Si			CIGS glass-glass			CIGS glass-aluminum		
	STC	1×	2.2×	STC	1×	2.2×	STC	1×	2.2×
I_{sc} (A)	8.9	7.3	15.4	2.5	1.9	4.4	5.9	4.6	8.9
V_{oc} (V)	38.0	34.3	32.9	44.0	40.8	39.6	3.14	2.98	2.95
FF (%)	75.2	72.4	66.9	72.9	71.6	68.0	57.1	56.3	62.4
P_{max} (W)	255	182	339	80	58	118	10.6	7.7	13.9
G (W·m^{-2})	1000	821	1729	1000	796	1777	1000	784	1524
T_{mod} (°C)	25	44.6	51.9	25	50.3	59.6	25	41.7	45.2

Fig. 10. I–V curve in outdoor conditions (2.2× and 1×) compared to STC, for the LCPV prototypes: a) c-Si; b) CIGS glass-glass; c) CIGS glass-aluminum.
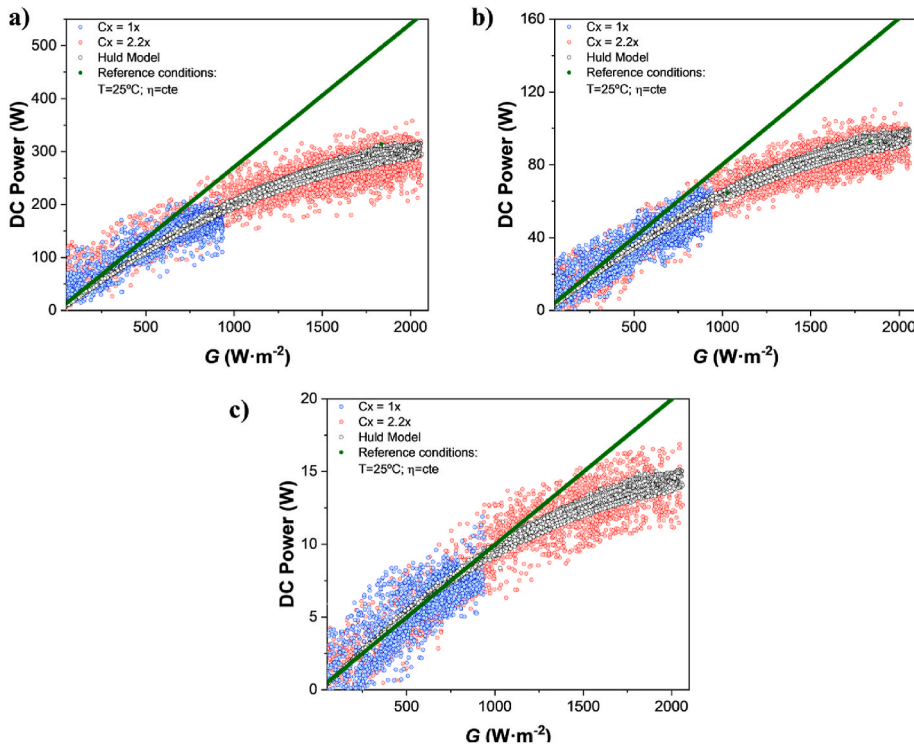

Fig. 11. DC output power monitored in outdoor conditions under LCPV conditions considering different PV technologies: a) c-Si, b) CIGS glass-glass, and c) CIGS glass-aluminum.

glass with an aluminum heat sink in CIGS technology, we observed a further enhancement in its performance under LCPV conditions. This improvement highlights the significance of thermal management strategies in optimizing CIGS-based LCPV systems. The maximum relative difference between the temperature of the CIGS module and the ambient temperature is less than 20 °C for the glass-aluminum encapsulation,

while the glass-glass encapsulated CIGS prototype exhibited a maximum relative temperature difference of 35 °C. The replacement of the back glass with an aluminum sheet, serving as a passive heater dissipator, represents a clear advantage in terms of design operation conditions.

In summary, this research study provides insights into the advantages of CIGS technology for LCPV systems, emphasizing the importance
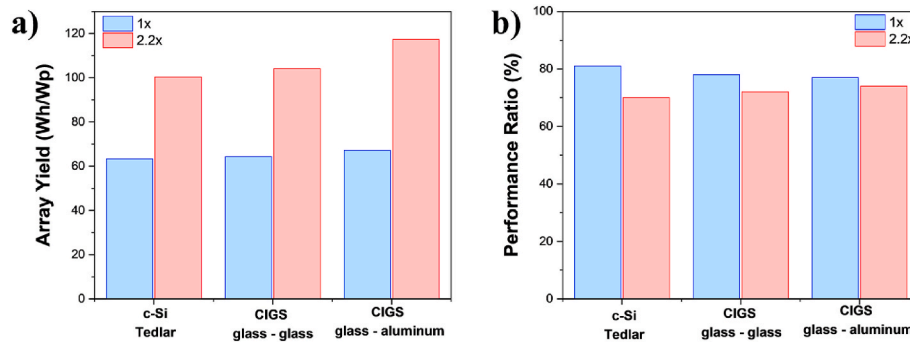
Fig. 12. a) Array Yield; b) Performance Ratio of each prototype.

of considering both the Voc temperature coefficient and encapsulation strategies for maximizing photovoltaic production.

CRediT authorship contribution statement

Miguel Barragán Sánchez-Lanuza: Writing – review & editing, Writing – original draft, Validation, Software, Data curation. **Isidoro Lillo-Bravo:** Writing – review & editing, Writing – original draft, Validation, Supervision, Software, Resources, Methodology, Investigation, Formal analysis, Conceptualization. **Sara Moreno-Tejera:** Software, Formal analysis, Data curation. **J.L. Sancho Rodríguez:** Validation, Formal analysis, Data curation. **Jose-Maria Delgado-Sanchez:** Writing – review & editing, Writing – original draft, Validation, Software, Methodology, Investigation, Formal analysis, Data curation, Conceptualization.

Declaration of competing interest

The authors declare that they have no known competing financial interests or personal relationships that could have appeared to influence the work reported in this paper.

Data availability

Data will be made available on request.

References

Baharoon, D.A., Rahman, H.A., Omar, W.Z.W., Fadhl, S.O., 2015. Historical development of concentrating solar power technologies to generate clean electricity efficiently – a review. Renew. Sustain. Energy Rev. 41, 996–1027.

Cherif, F.E., Sammouda, H., 2022. Prediction of the power conversion efficiency of Perovskite-on-CIGS tandem and triple junction thin-film under solar concentration irradiations by optimization of structural and optoelectronic materials characteristic. Mater. Sci. Eng., B 280, 115712.

Dierauf, T., Growitz, A., Kurtz, S., Hansen, C., 2013. Weather-corrected Performance Ratio Technical Report NREL/TP-5200-57991, pp. 1–6. Technical Report NREL/TP-5200-57991 (April NREL/TP-5200-57991).

Famoso, F., Lanzafame, R., Maenza, S., Scandura, P.F., 2015. Performance comparison between Low Concentration Photovoltaic and fixed angle PV systems. Energy Proc. 81, 516–525.

Fernández-Solas, A., Micheli, L., Almonacid, F., Fernández, E.F., 2021. Optical degradation impact on the spectral performance of photovoltaic technology. Renew. Sustain. Energy Rev. 141, 110782.

Grosjean, A., Soum-Glaude, A., Thomas, L., 2021. Replacing silver by aluminum in solar mirrors by improving solar reflectance with dielectric top layers. Sustainable Materials and Technologies 29, e00307.

Huld, T., Gottschalg, R., Beyer, H.G., Topic, M., 2010. Mapping the performance of PV modules, effects of module type and data averaging. Sol. Energy 84 (2), 324–338.

Huld, T., Friesen, G., Skoczek, A., Kenny, R.P., Sample, T., Field, M., Dunlop, E.D., 2011. A power-rating model for crystalline silicon PV modules. Sol. Energy Mater. Sol. Cell. 95, 3359–3369.

Khalid, A.M., Mitra, I., Warmuth, W., Schacht, V., 2016. Performance Ratio – crucial parameter for grid connected PV plants. Renew. Sustain. Energy Rev. 65, 1139–1158.

Kolamroudi, M.K., Ilkan, M., Egelioglu, F., Safaei, B., 2022. Maximization of the output power of low concentrating photovoltaic systems by the application of reflecting mirrors. Renew. Energy 189, 822–835.

Lee, H., Jung, M.-C., Lee, D.H.D., Han, M.J., 2023. First-principles theory-based design of highly reflective metals for radiative cooling. Curr. Appl. Phys. 49, 1–5.

Li, G., Xuan, Q., Pei, G., Su, Y., Ji, J., 2018. Effect of non-uniform illumination and temperature distribution on concentrating solar cell – a review. Energy 144, 1119–1136.

Luque, A., Hegedus, S., 2010. "Handbook of Photovoltaic Science and Engineering", second ed. John Wiley & Sons Ltd., West Sussex.

Mansoor, M., Simon, S.P., Kumar, K.A., Sundareswaran, K., Nayak, P.S.R., Padhy, N.P., 2020. "Impact and Economic Assessment on Solar PV Mirroring System – A Feasibility Report", vol. 203. Energy Conversion and Management, 112222.

Nyarko, F.K.A., Takyi, G., Amalu, E.H., Adaramola, M.S., 2019. Generating temperature cycle profile from in-situ climatic condition for accurate prediction of thermo-mechanical degradation of c-Si photovoltaic module. Engineering Science and Technology 22 (2), 502–514.

Oufettoul, H., Lamdihine, N., Motahhir, S., Lamrini, N., Abdelmoula, I.A., Aniba, G., 2023. Comparative performance analysis of PV module positions in a solar PV array under partial shading conditions. IEEE Access 11, 12176–12194.

Parupudi, R.V., Singh, H., Kolokotroni, M., 2020. Low concentrating photovoltaics (LCPV) for buildings and their performance analyses. Appl. Energy 279, 115839.

Peng, J., Lu, L., Yang, H., Ma, T., 2015. Validation of the Sandia model with indoor and outdoor measurements for semi-transparent amorphous silicon PV modules. Renew. Energy 80, 316–323.

Reis, F., Brito, M.C., Corregidor, V., Wemans, J., Sorasio, G., 2010a. Modeling the performance of low concentration photovoltaic systems. Sol. Energy Mater. Sol. Cell. 94 (7), 1222–1226.

Reis, F., Brito, M.C., Corregidor, V., Wemans, J., Sorasio, G., 2010b. Modeling the performance of low concentration photovoltaic systems. Sol. Energy Mater. Sol. Cell. 94 (7), 1222–1226.

Saini, V., Tripathi, R., Tiwari, G.N., Al-Helal, I.M., 2018. Electrical and thermal energy assessment of series connected N partially covered photovoltaic thermal (PVT)-compound parabolic concentrator (CPC) collector for different solar cell materials. Appl. Therm. Eng. 128, 1611–1623.

Shams, A., 2022. Influence of photovoltaic cell technologies and elevated temperature on photovoltaic system performance. Eng. J. 14 (7), 101984.

Shanks, K., Senthilarasu, S., Mallick, T.K., 2016. Optics for concentrating photovoltaics: trends, limits and opportunities for materials and design. Renew. Sustain. Energy Rev. 60, 394–407.

Shockley W., Queisser H.J., "Detailed balance limit of efficiency of p-n junction solar cells" (1961), J. Appl. Phys. 32(3), pp. 510-519.

Wang, A., Xuan, Y., 2020. Multiscale prediction of localized hot-spot phenomena in solar cells. Renew. Energy 146, 1292–1300.

Wang, Z., Kortge, D., Zhu, J., Zhou, Z., Torsina, H., Lee, C., Bermel, P., 2020. Lightweight, passive radiative cooling to enhance concentrating photovoltaics. Joule 4, 2702–2717.

Ward, J.S., Ramanathan, K., Hasoon, F.S., Coutts, T.J., Keane, J., Contreras, M.A., Moriarty, T., Noufi, R., 2002. A 21.5% efficient Cu(In,Ga)Se$_2$ thin-film concentrator solar cells. Prog. Photovoltaics Res. Appl. 10, 40–46.

Wennerberg, J., Kessler, J., Hedström, J., Stolt, L., Karlsson, B., Rönnelid, M., 2000. Thin film PV modules for low concentration systems. Sol. Energy 69 (1–6), 243–255.

Woyter, A., Richter, M., Moser, D., Green, M., Mau, S., Beyer, H.G., 2014. "Analytical Monitoring of Grid-Connected Photovoltaic Systems" https://doi.org/10.13140/2.1.1133.6481. *Report IEA-PVPS T13-03.*

Yadav, P., Tripathi, B., Lokhande, M., Kumar, M., 2013. Estimation of steady state and dynamic parameters of low concentration photovoltaic system. Sol. Energy Mater. Sol. Cell. 112, 65–72.

Yang, M., Wang, Z., Chen, L., Tang, W., 2020. Dynamic heat transfer model of flat plate solar water collectors with consideration of variable flow rate. Sol. Energy 212, 34–47.

Yolcan, O.O., Kose, R., 2023. Photovoltaic module cell temperature estimation: developing a novel expression. Sol. Energy 249, 1–11.

Zahedi, A., 2011. Review of modelling details in relation to low-concentration solar concentrating photovoltaic. Renew. Sustain. Energy Rev. 15, 1609–1614.